Iron Oxide-Decorated Carbon for Supercapacitor Anodes with Ultrahigh Energy Density and Outstanding Cycling Stability

Cao Guan,*,† Jilei Liu,‡ Yadong Wang,§ Lu Mao,† Zhanxi Fan,⊥ Zexiang Shen,‡ Hua Zhang,⊥ and John Wang*,†

†Department of Materials Science and Engineering, National University of Singapore, 117574 Singapore, ‡School of Physical and Mathematical Sciences, Nanyang Technological University, 637371 Singapore, §School of Engineering, Nanyang Polytechnic, 569830 Singapore, and ⊥School of Materials Science and Engineering, Nanyang Technological University, Singapore 639798, Singapore

ABSTRACT Supercapacitor with ultrahigh energy density (e.g., comparable with those of rechargeable batteries) and long cycling ability (>50000 cycles) is attractive for the next-generation energy storage devices. The energy density of carbonaceous material electrodes can be effectively improved by combining with certain metal oxides/hydroxides, but many at the expenses of power density and long-time cycling stability. To achieve an optimized overall electrochemical performance, rationally designed electrode structures with proper control in metal oxide/carbon are highly desirable. Here we have successfully realized an ultrahigh-energy and long-life supercapacitor anode by developing a hierarchical graphite foam−carbon nanotube framework and coating the surface with a thin layer of iron oxide (GF−CNT@Fe_2O_3). The full cell of anode based on this structure gives rise to a high energy of ~74.7 Wh/kg at a power of ~1400 W/kg, and ~95.4% of the capacitance can be retained after 50000 cycles of charge−discharge. These performance features are superior among those reported for metal oxide based supercapacitors, making it a promising candidate for the next generation of high-performance electrochemical energy storage.

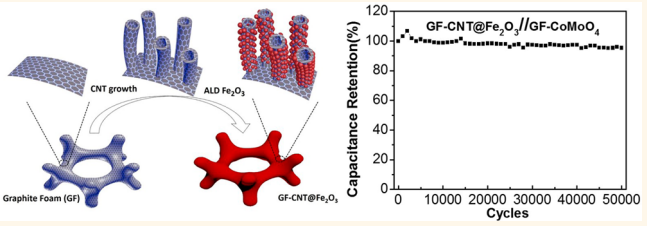

KEYWORDS: metal oxide · supercapacitor anode · energy density · cycling stability · atomic layer deposition

Supercapacitors, which bridge the storage gap between high energy batteries and high power dielectric capacitors, have been considered as an important class of energy source for high power supplies, electric and hybrid vehicles, and portable electronics.[1] A basic supercapacitor is composed of two electrodes, electrolyte, and separator between the electrodes, in which the electrode materials are playing a decisive role in the overall electrochemical performance. Supercapacitor electrode materials can be divided into two main groups: carbonaceous materials (such as carbon nanotubes, graphene, and active carbons) and pseudocapacitive materials (such as transition-metal oxides/hydroxides and conducting polymers).[2] As a traditional electrode, carbonaceous materials can offer very high power density (a power density of more than 75 KW/kg has been demonstrated with an organic electrolyte[3]) and excellent cycling ability (up to 10000 cycles).[4] However, the typical energy density of carbon-based materials (e.g., 4−5 Wh/kg for active carbon) is still too low, compared with common rechargeable batteries (more than 180 Wh/kg for lithium ion batteries).[3,4] In the past decade, tremendous research efforts have been devoted to developing supercapacitors with high energy density in order to meet the growing demands for both high power density and high energy density and fulfill the requirement for next-generation energy storage devices.[5,6]

To develop high energy density electrodes, transition-metal oxides/hydroxides have drawn specific attention since they can offer much higher energy densities (with Faradaic reactions) than those of carbon-based materials.[7,8] However, there are obvious drawbacks of these metal oxides, such as

* Address correspondence to msegc@nus.edu.sg, msewangj@nus.edu.sg.

Received for review January 26, 2015 and accepted April 13, 2015.

Published online April 13, 2015
10.1021/acsnano.5b00582

low electric conductivity, poor rate performance, and limited cycling ability.[9,10] Several strategies have therefore been devised in order to achieve high energy for oxide-based supercapacitor electrodes. For example, nanosized materials of metal oxides, especially those with mesoporous and hollow features, have been fabricated,[11−13] where the downsized materials provide much higher surface area for better electrode−electrolyte contact and short ion-diffusion length, thus enabling fast redox reaction at high rates. Several nanostructures have been demonstrated to be effective, such as nanoparticles,[14] nanowires,[15] porous nanoflakes,[16] and hollowed nanospheres.[17] An alternative approach is to combine metal oxides with carbonaceous materials and/or conducting polymers for better overall electrochemical performance, since the carbon materials can improve the electric conductivity and contribute to the rate and cycling ability.[18,19] With this consideration, several different types of hybrid structures (such as core−shell, core−branch, and sandwiched structures of carbon and metal oxide materials) have been reported, with some demonstrating improvement in energy density.[20−27] Other approaches for achieving high energy density for metal oxide electrodes include the development of binder-free materials,[28,29] conductive surface coating,[30−32] and surface modification.[33]

Despite considerable efforts with metal oxides, there are still several challenges that need to be addressed in order to realize the most desirable electrode.[8,34,35] First and foremost, although the metal oxides/hydroxides can in theory lead to high energy density, in many cases the power density is largely sacrificed due to their poor electrical conductivity and insufficient electron transfer at high rates, especially when the mass content of metal oxides/hydroxides is high. Thus, one of the main issues with metal oxides/hydroxides is the high power, which requires a proper structure design and an optimized mass loading in order to balance the energy and power density.[8] The second major challenge with these high energy metal oxide materials is the cycling stability.[7] Currently commercially available carbon-based supercapacitors can be cycled up to 100000 cycles. The reported results for metal oxides electrodes cannot reach a level close to this (normally below 10000 cycles). The poor cycling ability may well be originated from the long-time Faradaic reaction of metal oxides, which brings about considerable physiochemical change/strain on electrode materials; thus, they cannot maintain the fully electrochemical active state for a long period of time. Although nanosized materials have shown potential improvement, they remain a big challenge to developing metal oxide electrodes with excellent cycling ability for long-term practical usage.[36] Third, high-energy density requires a large mass loading/content of active materials in supercapacitors.[3,34,37] Most of the energy/power densities reported for supercapacitors are only based on the active materials. However, in practical application, these key parameters shall be based on the weight/volume of the whole device including the package and nonactive material substrates. Indeed, the nonactive material substrate can be heavy in weight and large in volume (for example, nickel foil and nickel foam usually have mass loadings of 30−50 mg/cm^2), which can be more than 10 times that of the active material mass. It is thus a big challenge to develop "truly" high energy and high power with a low content of nonactive materials,[35] yet the supercapacitor performance can be drastically deteriorated by reducing or eliminating the use of these nonactive but conductive/stable substrate.

With the above consideration, in this work we describe a novel hierarchical structure consisting of iron oxide nanoparticles decorated on a three-dimensional (3D) ultrathin graphite foam−carbon nanotube forest substrate (noted as GF−CNT@Fe_2O_3). The integrated structure owns several advantages when utilized as a supercapacitor anode. For example, the graphite foam−CNT forest (deposited by chemical vapor deposition (CVD) method and noted as GF−CNT) can be utilized as a flexible, lightweight, conducive substrate with robust mechanical stability. Its superior performance as supercapacitor substrate has been identified in our recent work.[38,39] Without other conductive support or polymer-binder being required, it can drastically reduce the nonactive material mass. Iron oxide, a low-cost high capacitance anode material,[40−43] is then deposited on the GF−CNT by atomic layer deposition (ALD). The amount of Fe_2O_3 deposited can be well controlled for optimizing the electrochemical performance.[44,45] ALD is shown to be effective in developing material of high uniformity with conformal features, especially for substrates with a high-aspect ratio and complex morphology.[46−49] The GF−CNT@Fe_2O_3 demonstrates ultrahigh specific capacitance and ultralong cycling ability, which are superior compared with those previously reported for iron oxide/carbon anodes.[50,51] In addition, a full cell with the GF−CNT@Fe_2O_3 anode and GF−$CoMoO_4$ cathode is shown with high energy density and long-time cycling stability at high rate, which indeed compares favorably with the previously reported performance for metal oxides based full cells.[57−59] The strategy of effectively decorating metal oxides on highly porous, lightweight, but conductive carbon support can also be extended to the combination of other pseudocapacitive materials and carbon substrates for the next-generation high-energy supercapacitors.

RESULTS AND DISCUSSION

Fabrication and Physical Characterization. As illustrated in Scheme 1, GF−CNT was first made using a CVD

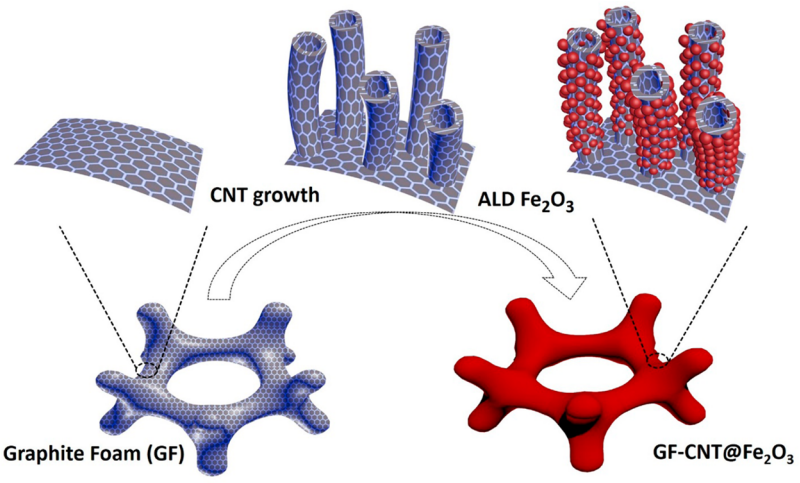

Scheme 1. Growth Procedure of GF−CNT@Fe_2O_3 Starting from Graphite Foam

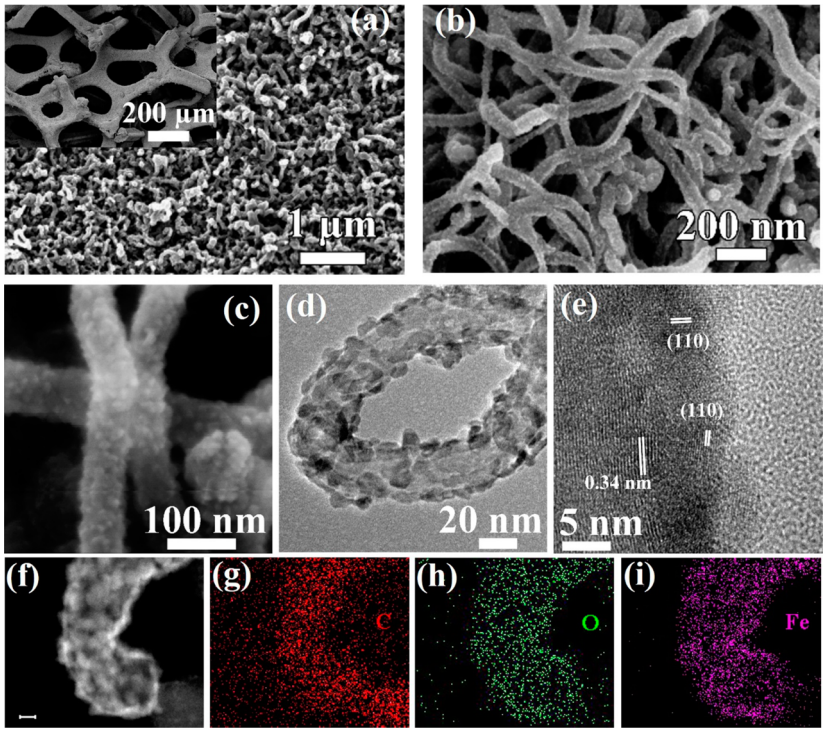

Figure 1. SEM and TEM characterization of GF−CNT@Fe_2O_3. (a−c) SEM and (d−e) HRTEM images of GF−CNT@Fe_2O_3. (f) HAADF−STEM image of a single CNT@Fe_2O_3 and (g−i) the corresponding STEM element mapping. The scale bar in (f) is 10 nm.

method according to our previous report, where a CVD ultrathin graphite foam is used as substrate and Co−Ni catalyst is adopted to synthesize CNTs forest on the graphite foam.[38] The GF−CNT has been demonstrated to exhibit high electrical conductivity, high surface area, and mechanical flexibility.[38] In this work, to further enhance the energy density, the GF−CNT substrate was coated with nanocrystalline Fe_2O_3, a promising low-cost anode material with high theoretic capacitance. ALD is adopted for the deposition of Fe_2O_3 since it gives rise to high uniformity in texture and the deposition amount can be well-controlled. With the ALD coating, a hierarchical structure of GF−CNT@Fe_2O_3 is developed. A SEM image of the GF−CNT@Fe_2O_3 is shown in Figure 1a, from which one can see the 3D graphite foam has been covered with many wire-shaped structures and the one-dimensional structure of CNT is well maintained after the process. The high magnification image in inset shows that the foam structure is also well-preserved after the ALD coating. Enlarged images in Figure 1b,c clearly show the CNTs have been uniformly coated with many small nanoparticles, and no aggregation can be observed. From these SEM images, one can see nanocrystalline Fe_2O_3 has been uniformly deposited on the structure of graphite foam with CNT forest, and the

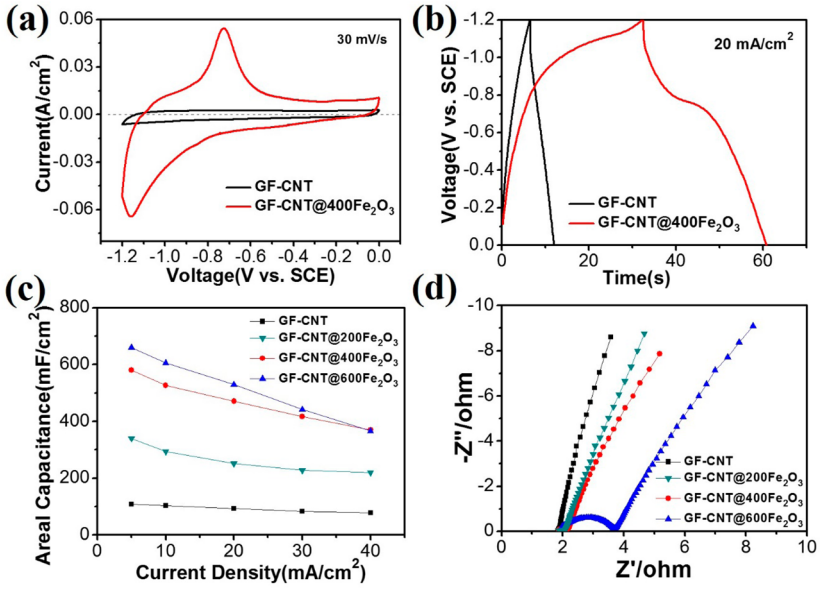

Figure 2. (a) CV curves and (b) charge−discharge curves of GF−CNT@400Fe_2O_3 and GF−CNT. (c) Rate properties and (d) EIS of four samples.

GF−CNT is well preserved during the ALD process. It is noted that the Fe_2O_3 loading can be easily tuned by controlling the number of ALD cycles. In the present work, three samples were prepared with ALD cycles of 200, 400, and 600, respectively (noted as GF−CNT@200Fe_2O_3, GF−CNT@400Fe_2O_3, and GF−CNT@600Fe_2O_3). HRTEM images of typical CNT@Fe_2O_3 are shown in Figure 1d,e. From Figure 1d, one can see that CNT is uniformly covered with tiny nanoparticles (typical particle sizes are ~10 nm). The fine-sized particles facilitate the access of electrolyte to large surface area and are thus desirable for high capacitance and high power of superacpacitor electrode.[16] The HRTEM image of CNT@Fe_2O_3 in Figure 1e clearly shows crystallinity of the CNT (with a typical lattice distance of 0.34 nm) and Fe_2O_3 (hematite JPCD: 33-664, matches well with those of previous reports[52,53]). The chemical composition of CNT@Fe_2O_3 is further illustrated by the HAADF−STEM image (Figure 1f) and the corresponding elemental mapping (Figure 1g−i). From the mapping result, the Fe and O are uniformly distributed on the CNT, further confirming the conformal coating of Fe_2O_3 nanoparticles. It is also noted that nanocrstalline Fe_2O_3 is assembled on the CNT surface with an island growth mode, which is different from the previous report of ZnO@Fe_2O_3[44] and CNT@V_2O_5,[54] where the ALD metal oxides were in a 2D growth mode. It is also different from the Fe_2O_3 deposited on TiO_2 nanotubes (see Figure S1, Supporting Information). The difference can be attributed to the different surface characteristics of CNTs compared to other materials and different substrates.[55−57] The growth per cycle of Fe_2O_3 on CNT substrate is determined ~0.25 Å in the present study, which is ~50% of that for flat substrate (~0.5 Å). The rather inert surface of CNT reduces the growth rate of ALD deposition,[58,59] and surface modification can result in a higher growth rate and different growth mode.[58,59] In the present study, the CNTs are used "as received", and no further modification was made.

X-ray photoelectron spectroscopy (XPS) is conducted to study the GF−CNT@Fe_2O_3, and the results are shown in Figure S2 (Supporting Information). From the wide-range scan in Figure S2a (Supporting Information) for GF−CNT@Fe_2O_3, one can see the electronic state of three elements (Fe, O, and C), and no other impurities are detected. From the Fe 2p spectrum in Figure S2b (Supporting Information), two peaks (Fe 2p 3/2 and 2p 1/2) are located at 710.8 and 724.4 eV accompanied by a broad satellite peak, respectively. The result matches well with the previous report of Fe^{3+}, and no other Fe^{2+} state has been observed.[44,45] In Figure S2c (Supporting Information), the principal peak of O 1s is centered approximately at 530.3 eV, which is attributed to the metal oxide form (O^{2-}). The small shoulder located at 531.1 eV is originated from the surface −OH group. In the C 1s spectrum in Figure S2d (Supporting Information), the peak centered at 284.5 eV corresponds to the C−C bond, and the small peaks at 286.2 and 288.5 eV are assigned to C−O and C═O bonds, respectively.[50] Raman and XRD experiment further confirm the crystal structure of GF−CNT@Fe_2O_3; detailed discussions are in the Supporting Information.

Three-Electrode Tests. The electrochemical behavior of GF−CNT@Fe_2O_3 is studied using a three-electrode system with 2 M KOH as the electrolyte. Figure 2a shows the CV cures of bare GF−CNT and GF−CNT@400Fe_2O_3, from which one can see that the bare GF−CNT has a rather rectangular curve, typically

for electric double-layer capacitance, while the CV curve of GF−CNT@400Fe_2O_3 has apparent redox peaks (pseudocapacitive behavior). The enclosed area of GF−CNT@400Fe_2O_3 is also much larger than that of bare GF−CNT, showing the capacitance is significantly increased after the Fe_2O_3 coating. The reduction peak at ∼1.1 V and oxidation peak at ∼0.7 V can be well-defined as the pseudocapacitance from the reaction between Fe^{3+} and K^+ species in the electrolyte.[51,60] The charge−discharge curves shown for the two samples in Figure 2b also depict the capacitance increase after the Fe_2O_3 coating. At the same current density of 20 mA/cm^2, GF−CNT@400Fe_2O_3 expresses an areal capacitance of ∼470.5 mF/cm^2, which is ∼4 times larger than that of GF−CNT (∼93.8 mF/cm^2). After the ALD Fe_2O_3 coating, the areal capacitance of the carbon support is largely enhanced. Since the pseudoreaction takes place predominately on the surface and in the near-surface region of the metal oxides, and the Fe_2O_3 is rather insulating, it would be of interest to comprehensively investigate the relationship between the amount (controlled by ALD cycles) of Fe_2O_3 and the electrochemical performance. It may pave a way for achieving optimized supercapacitor performance and understanding the key phenomenon behind.

The CV curves of all four samples (GF−CNT, GF−CNT@200Fe_2O_3, GF−CNT@400Fe_2O_3, and GF−CNT@600Fe_2O_3) are shown in Figure S3 (Supporting Information), from which one can see that all samples with ALD Fe_2O_3 coating show larger capacitance than that of the bare GF−CNT, demonstrating the enhancement by ALD coating of pseudocapacitive materials. However, their electrochemical performances are quite different. The GF−CNT@200Fe_2O_3 shows apparent redox peaks similar to that of GF−CNT@400Fe_2O_3, but the peak current density is much smaller, which is expected as a smaller Fe_2O_3 mass gives rise to less Faradaic reaction. On the other hand, when the ALD cycles of Fe_2O_3 is increased to 600 cycles (more mass loading), the current density of the redox peaks did not increase much as compared with that of GF−CNT@400Fe_2O_3 (which means a slight increase in capacitance), yet the voltage difference between the oxidation and the reduction peak is larger, showing a decreased ionic and electronic conductivity due to the thicker Fe_2O_3 coating. Therefore, the mass loading of Fe_2O_3 is an important parameter in determining the capacitance. To achieve optimized electrochemical performance, the amount of Fe_2O_3 should be controlled as any excess loading will delay the electrochemical reaction thus sacrifice power density. By comparison, GF−CNT@400Fe_2O_3 appears to show the best electrochemical performance.

The rate capability of the four samples has been studied, and the results are shown in Figure 2c. When the charge−discharge current density changes from 5 to 40 mA/cm^2, the GF−CNT illustrates the best capacity retention (72.4% of the capacitance is maintained). However, since only electric double-layer capacitance is involved in this material, its absolute capacitance is the lowest. Upon depositing Fe_2O_3 with 200 ALD cycles, the areal capacitance is increased by ∼2−3 times. The rate capability is, however, sacrificed with 65.1% of capacitance retention. Further increase in the ALD amount of Fe_2O_3 results in higher areal capacitance, yet the capacitance retention for GF−CNT@400Fe_2O_3 drops to 63.8%. GF−CNT@600Fe_2O_3 delivers the highest areal capacitance of 659.5 mF/cm^2 at a current of 5 mA/cm^2. It drops very fast when the current density is increased to 40 mA/cm^2, which is even lower than that of GF−CNT@400Fe_2O_3, showing the poor rate ability at higher Fe_2O_3 content. Electrochemical impendence spectroscopy (EIS) shows a similar trend. As illustrated by Nyquist plots in Figure 2d, in the high frequency region, the semicycle diameter in real part gradually increases with the increasing number of ALD cycles of Fe_2O_3, indicating the charge-transfer resistance is increased by the thicker Fe_2O_3 layer. In the low frequency region, the slope of the curve represents the electrolyte and proton diffusion resistance. The GF−CNT shows the most ideal straight lines along the imaginary axis. The curve slope decreases with increasing number of Fe_2O_3 ALD cycles, indicating higher resistance for ion/proton diffusion. From the EIS study, it appears that a thicker Fe_2O_3 coating largely increases the resistance for charge transfer and ion diffusion; thus, the Faradaic reaction will be slowed down with low power, which agrees well with the results of rate capability.

As a key parameter of supercapacitor performance, the cycling ability of Fe_2O_3-coated GF−CNT is further studied and the results are shown in Figure 3a−c. The first and last two cycles for GF−CNT@400Fe_2O_3 are shown in Figure 3d,e. It is of interest to note that all three samples deliver excellent cycling ability, which can maintain 93.5%, 111.2%, and 86.2% of the initial capacitance even after 50000 cycles of charge−discharge at the current density of 20 mA/cm^2. The cycling ability of the ALD Fe_2O_3-coated GF−CNT is therefore much better than most of those reported for iron oxides/carbon-based materials.[50,51] Few iron-based oxides are cycled up to 10000 cycles, as summarized in Table S1 (Supporting Information). Although the exact reasons for the much improved cycling ability are not yet clear, we have considered the following parameters that can contribute to the overall cycling stability. (i) The structure of Fe_2O_3 nanoparticles on CNT is mechanically stable; otherwise, the Fe_2O_3 nanoparticles would be "blown away" during the ALD purge process. This mechanically stability is also shown by the well-preserved structure observed in TEM experiment, where ultrasonic was used in TEM sample preparation. (ii) Fe_2O_3 is in a refined nanocrystallite form, which exhibits a lower charge-transfer resistance

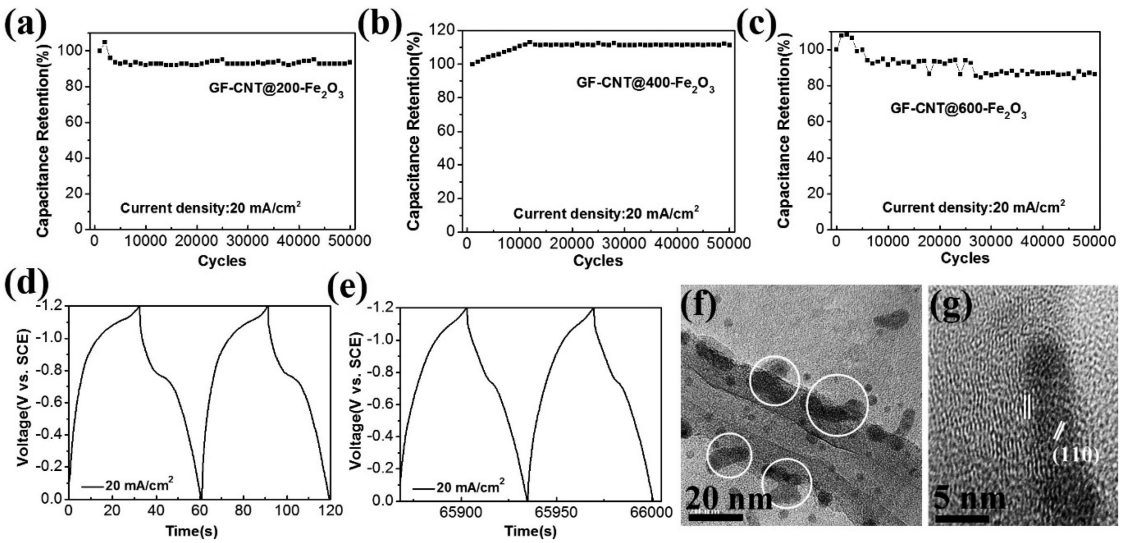

Figure 3. (a–c) Cycling tests of three samples with ALD Fe_2O_3 coating. (d, e) First and last two cycles of GF–CNT@400Fe_2O_3 during the cycling test. (f, g) TEM images for GF–CNT@400Fe_2O_3 after 50000 cycles. The TEM image in (f) shows the feature change and aggregation of the particles, and the HRTEM image in (g) shows crystalline Fe_2O_3 can be still observed.

and shorter ion/proton diffusion path compared with large nanowires or nanoparticles. It can thus better maintain the long-time reversible reactions and keep the electrode integrity.[61] (iii) There is enough free space between the Fe_2O_3 nanocrystallites; thus, the mechanical strain and volume expansion generated by the fast and long-time Faradaic reaction are effectively buffered.[9] This point has been further confirmed by TEM experiment after the cycling as discussed later. (iv) In our previous study, the GF–CNT is mechanically and electrochemically stable;[38] thus the long cycling ability of the GF–CNT@ Fe_2O_3 can also benefit from the stable substrate of GF–CNT. If the substrate is fragile, the hierarchical structure could not maintain the cycling ability in the long-time cycling test. To further understand the excellent cycling ability, a TEM experiment was conducted on the sample after a 50000 cycles test. From the typical TEM image shown in Figure 3f,g, one can see the core–shell structure is well-preserved, although the nanoparticles are somehow slightly aggregated. Similar phenomenon of aggregations of Fe_2O_3 nanoparticles in electrochemical reaction were observed, which was believed to shorten the cycling life of Fe_2O_3.[62] In the present work, nevertheless, the overall degree of particle aggregation is rather small (~20–30 nm), suggesting that the aggregation is alleviated.[62] This supports the stability of electrochemical activity of the GF–CNT@Fe_2O_3.

The above three-electrode electrochemical tests demonstrate that the GF–CNT@Fe_2O_3 is a rather stable supercapacitor anode with high capacitance and excellent rate capability. To evaluate its application for high-energy density supercapacitor, a full cell was constructed with the GF–CNT@Fe_2O_3 as anode and a $CoMoO_4$ nanohoneycomb on graphite foam (GF–$CoMoO_4$) as cathode. The GF–$CoMoO_4$ cathode is a metal oxide-based lightweight material which can express high pseudocapacitance in alkaline electrolyte. The SEM image of the GF–$CoMoO_4$ is shown in Figure S4a,b (Supporting Information), from which one can see the highly porous honeycomb structure of nanosheets is assembled on the graphite foam, where there is open space formed between the porous sheets. The electrochemical performance of GF–$CoMoO_4$ is further tested using a three-electrode system with 2 M KOH electrolyte. Its CV curves in Figure S4c (Supporting Information) clearly show the pseudoreaction of GF–$CoMoO_4$ in alkaline electrolyte, with a pair of redox peaks located around 0.3 V (vs SCE). Its charge–discharge curves are shown in Figure S4d, and the corresponding rate capability is shown in Figure S4e (Supporting Information). The specific capacitance of 2555.6 F/g (at 10 A/g) drops to 62.1% when the current density increases to 40 A/g. GF–$CoMoO_4$ also shows excellent cycling ability (Figure S4f, Supporting Information); i.e., there is little change in capacitance after 50000 cycles of charge–discharge at 20 A/g. The electrochemical performance measured for GF–$CoMoO_4$ in the present work is slightly different from that reported for $CoMoO_4$ nanohoneycomb–graphene foam,[36] due to the much higher mass loading (~2 times) in the present work. Nevertheless, in terms of the capacitance and long cycling ability, GF–$CoMoO_4$ is a good cathode choice for GF–CNT@Fe_2O_3 anode.

Full-Cell Test. Figure 4a shows the schematic illustration of the full-cell package, where the two electrodes are separated with an electrolyte-soaked separator and packed between two PET films. The digital images of single anode and prototype full-cell are shown in the insets of Figure 4c. Figure 4b shows the CV curves of GF–CNT@Fe_2O_3//GF–$CoMoO_4$ full device at different

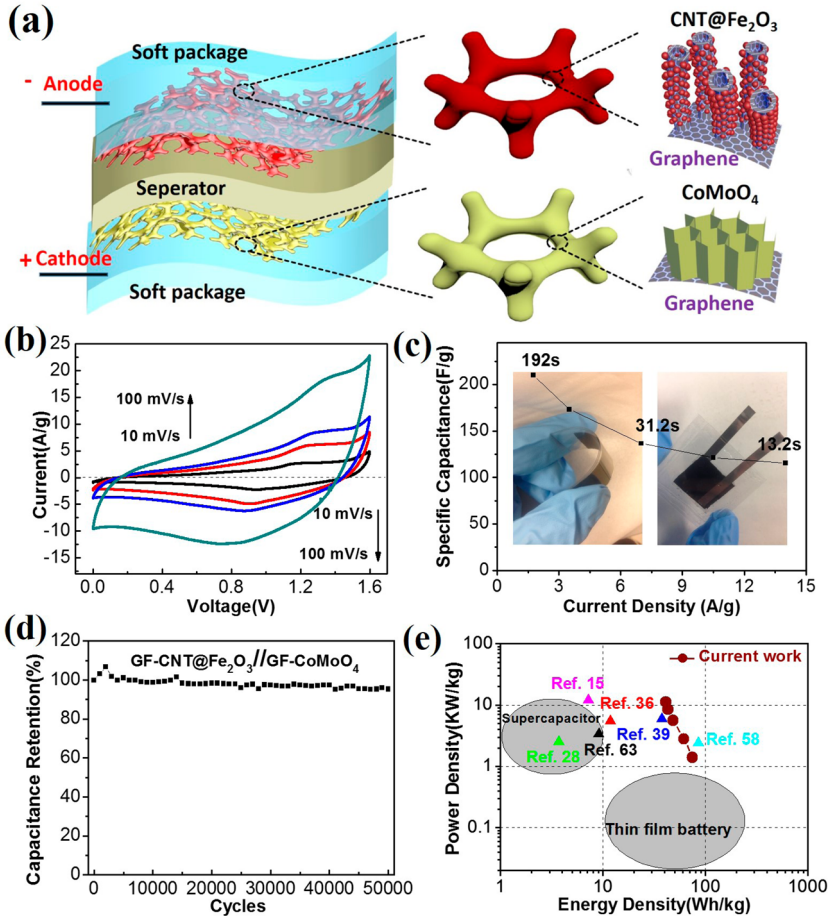

Figure 4. Electrochemical behavior of the GF−CNT@Fe_2O_3//GF−$CoMoO_4$ full cell. (a) Schematic of the full-cell package. (b) CV curves, (c) rate capability, (d) cycling ability with a current of 7 A/g, and (e) Ragone plot of the GF−CNT@Fe_2O_3//GF−$CoMoO_4$ full cell; some values reported from other ASCs are inserted in (e) for comparison. Insets in (c) are the digital photos of the single electrode and full cell.

scan rates within a cell voltage window of 0−1.6 V. A couple of redox peaks are observed, indicating the pesudoreaction from the electrodes ($Fe^0 \leftrightarrow Fe^{3+}$ and $Co^{2+} \leftrightarrow Co^{4+}$). Galvanostatic charge−discharge tests of the full-cell are conducted (Figure S5, Supporting Information), and the rate capability is shown in Figure 4c. Within a short discharge time of 192 s, the full cell can deliver a specific capacitance of ~210 F/g (based on the mass of the whole electrodes). When the current density further increases to 14 A/g, at a corresponding discharge time of only 13.2 s, the device could maintain a specific capacitance of ~115.5 F/g, showing the desirable rate performance. More interestingly, GF−CNT@Fe_2O_3//GF−$CoMoO_4$ also expresses excellent cycling ability, as shown in Figure 4d. Since both the electrodes exhibit excellent cycling stabilities, the full-cell was also tested for 50000 cycles at a current density of 7 A/g. Significantly, ~95.4% capacitance could be maintained after the large number of cycles. The cycling ability of GF−CNT@Fe_2O_3//GF−$CoMoO_4$ is much better than most of those reported for metal oxide-based full-cells[63−65] (see also from Table S2, Supporting Information). Indeed, it is comparable with those results achieved from pure carbon based full-cells. Based on the total mass of the electrode materials, the Ragone plot is shown in Figure 4e. GF−CNT@Fe_2O_3//GF−$CoMoO_4$ expresses a high energy density of ~74.7 Wh/kg at the power density of ~1.4 kW/kg. Even at a high power density of ~11.2 kW/kg, the cell can deliver a high energy density of ~41.1 Wh/kg. The combination of high energy and power densities of the GF−CNT@Fe_2O_3//GF−$CoMoO_4$ full device are compared favorably with those of iron oxide or $CoMoO_4$/carbon material based supercapacitors.[36,41] It is indeed superior among metal oxide based supercapacitors including those using organic electrolytes (see also from Table S2, Supporting Information), demonstrating the merits brought in by the rational design of hierarchical carbon−metal oxide nanostructure. By taking into account of the whole device mass being 50% of active materials,[51] GF−CNT@Fe_2O_3//GF−$CoMoO_4$ still delivers very high energy densities (~20.5−37.3 Wh/kg) without sacrificing much in power densities (~0.7−5.6 KW/kg).

To demonstrate the potential application of the GF−CNT@Fe_2O_3//GF−$CoMoO_4$ supercapacitor, three full

cells (each contains 3 × 3 cm^2 of GF−CNT@Fe_2O_3) are connected in series (not shown). This three-cell configuration (after charging) can easily light up 30 parallel orange light-emitting diodes (LEDs).

CONCLUSIONS

To conclude, we have successfully developed a novel iron oxide decorated 3D graphite foam−CNT forest hierarchical structure (GF−CNT@Fe_2O_3), processed by the combination of CVD (for carbon materials) and ALD (for metal oxide) techniques. By utilizing the high conductivity and porous structure of carbon materials and the controllable ALD metal oxide with high energy density, GF−CNT@Fe_2O_3 expresses ultrahigh capacitance and excellent cycling ability in supercapacitors. A full-cell with the GF−CNT@Fe_2O_3 anode and GF−$CoMoO_4$ cathode is demonstrated with "truly" high energy density without sacrificing the high power density and excellent cycling ability. The rational design concept for metal oxide/carbon nanocomposites can be extended to other metal oxides and carbon substrates, which can pave ways for ultrahigh energy density storage devices.

METHODS

Material Synthesis. (a) GF−CNT hierarchical structure is developed by modification of a previously reported method[38] where GF was synthesized by the CVD method using Nickel foam (8 × 8 × 0.2 cm^3) as substrate. CNT was fabricated using a NiCo catalyst with First Nano's EasyTube 300 System. A gas flow of C_2H_4, H_2, and Ar (flow rates is 20, 40, and 100 sccm, respectively) was used for the CNT growth at 750 °C. After the growth, samples were put into 3 M HCl (60 °C) to remove the catalyst, and the areal density of GF−CNT was adjusted to 0.65 mg/cm^2. (b) ALD Fe_2O_3 was conducted using a SUNALE R-200 ALD reactor (Picosun Oy) with $Fe(Cp)_2$ and O_3 (ozone concentration ~10%, generated in a 500 sccm mixture of oxygen (99.99%) and nitrogen (99.998%)) as sources for iron and oxygen, respectively. The $Fe(Cp)_2$ was held in a stainless steel bottle maintained at 165 °C, while the reaction chamber was maintained at 300 °C and 14 hPa during the reaction. The carrying and purge gas was nitrogen with a purity of 99.999%. Pulse time of iron precursor was controlled at 1.6 s with a boosting function, and each O_3 precursor exposure time is 0.2 s. Six second and 4 s N_2 purge steps were used after the iron and O_3 exposure, respectively. The ALD Fe_2O_3 thin film thickness on flat Si substrate was measured using spectroscopic ellipsometry (α-SE, J. A. Woollam). At 400 ALD Fe_2O_3 cycles, the resultant thin film thickness is about 20 nm, which presents a growth rate of ~0.05 nm per cycle. (c) GF−$CoMoO_4$ was synthesized following a reported hydrothermal method,[36] where $Co(NO_3)_2$ and $NaMoO_4$ were used as the sources, a GF foam was used as the substrate, and the mass of GF−$CoMoO_4$ is ~1 mg/cm^2.

Characterization. Samples were characterized using scanning electron microscopy (SEM, Zeiss, 5.0−20.0 kV), transmission electron microscopy (TEM, JEOL-2100F) with an EDX detector, X-ray photoelectron spectroscopy (XPS, AXIS Ultra), X-ray Diffraction (XRD, Bruker D8 diffractometer), Raman scattering spectra (LABRAM-HR Raman spectrometer, excited with 514.5 nm Ar^+ laser), and thermal gravimetric analysis (SDT Q600). The mass of electrode materials was also recorded by an AX/MX/UMX Balance (METTLER TOLEDO, maximum = 5.1 g; Δ = 0.001 mg).

Electrochemistry Measurement. Electrochemical measurements were performed using an electrochemical workstation (Solartron 1470E) at room temperature. For three-electrode system tests, GF−CNT@Fe_2O_3 or GF−$CoMoO_4$ was directly attached to a metal clip to be used as the working electrode, and no metal support or other current collector was used. A Pt plate and SCE were used as the counter electrode and the reference electrode, respectively. KOH (2 M) was used as the electrolyte. For two-electrode tests, GF−CNT@Fe_2O_3, an electrolyte-soaked separator, and GF−$CoMoO_4$ were packed using two PET sheets and sealed with a Lacor home vacuum pack.

The specific capacitance in the three-electrode system is calculated by $C = It/(\Delta Vm)$, and areal capacitance is calculated by $C_a = It/(\Delta VS)$, where I is the discharge current, t is the discharge time, ΔV is the voltage drop upon discharging, m is the individual electrode mass including the GF and CNT, and S is the geometrical area of the electrode.

To assemble a full cell, the following equation is used to balance the charge between the anode and cathode, $C^- * \Delta V^- * m^- = C^+ * \Delta V^+ * m^+$, where C (F/g) is the specific capacitance of single electrode, ΔV (V) is the working potential range, and m is the mass of the electrode.

The energy density (E) and power density (P) are calculated by $E = C_{cell}\Delta V^2/2$, $P = E/t$, where C_{cell} is the cell capacitance calculated by $C_{cell} = It/(\Delta Vm)$, ΔV is the voltage drop upon discharging, t is the discharge time, I is the discharge current, and m is the total mass of the two electrodes. To estimate the energy and power density of the whole device including the package mass, the m_{device} is estimated to be 2 times that of the electrode mass.

Conflict of Interest: The authors declare no competing financial interest.

Acknowledgment. This research is supported by the Agency for Science, Technology and Research (A*STAR, Singapore), Grant No. 1121202013, conducted at the National University of Singapore.

Supporting Information Available: Additional SEM−TEM images of CNT@Fe_2O_3, XPS, Raman, XRD results, TGA data, and detailed CV and charge−discharge curves of GF−CNT@Fe_2O_3, SEM images, and electrochemical behavior of GF−$CoMoO_4$. Summary of supercapacitor performance for FeOx and FeOx/carbon materials (Table 1). Comparison of electrochemical performance of metal oxides (focused on FeOx and $CoMoO_4$) based energy storage devices (Table 2). This material is available free of charge *via* the Internet at http://pubs.acs.org.

REFERENCES AND NOTES

1. Simon, P.; Gogotsi, Y. Materials for Electrochemical Capacitors. *Nat. Mater.* **2008**, *7*, 845–854.
2. Wang, G.; Zhang, L.; Zhang, J. A Review of Electrode Materials for Electrochemical Supercapacitors. *Chem. Soc. Rev.* **2012**, *41*, 797–828.
3. Zhu, Y.; Murali, S.; Stoller, M. D.; Ganesh, K. J.; Cai, W.; Ferreira, P. J.; Pirkle, A.; Wallace, R. M.; Cychosz, K. A.; Thommes, M.; et al. Carbon-Based Supercapacitors Produced by Activation of Graphene. *Science* **2011**, *332*, 1537–1541.
4. Zhang, L. L.; Zhao, X. S. Carbon-Based Materials as Supercapacitor Electrodes. *Chem. Soc. Rev.* **2009**, *38*, 2520–2531.
5. Hall, P. J.; Mirzaeian, M.; Fletcher, S. I.; Sillars, F. B.; Rennie, A. J. R.; Shitta-Bey, G. O.; Wilson, G.; Cruden, A.; Carter, R. Energy Storage in Electrochemical Capacitors: Designing Functional Materials to Improve Performance. *Energy Environ. Sci.* **2010**, *3*, 1238–1251.
6. Deng, W.; Ji, X.; Chen, Q.; Banks, C. E. Electrochemical Capacitors Utilising Transition Metal Oxides: An Update of Recent Developments. *RSC Adv.* **2011**, *1*, 1171–1178.

7. Simon, P.; Gogotsi, Y.; Dunn, B. Where Do Batteries End and Supercapacitors Begin? *Science* **2014**, *343*, 1210–1211.
8. Augustyn, V.; Simon, P.; Dunn, B. Pseudocapacitive Oxide Materials for High-Rate Electrochemical Energy Storage. *Energy Environ. Sci.* **2014**, *7*, 1597–1614.
9. Liu, C.; Li, F.; Ma, L.-P.; Cheng, H.-M. Advanced Materials for Energy Storage. *Adv. Mater.* **2010**, *22*, E28–E62.
10. Xia, X.; Zhang, Y. Q.; Chao, D.; Guan, C.; Zhang, Y.; Li, L.; Ge, X.; Bacho, I. M.; Tu, J.; Fan, H. J. Solution Synthesis of Metal Oxides for Electrochemical Energy Storage Applications. *Nanoscale* **2014**, *6*, 5008–5048.
11. Zhao, X.; Sanchez, B. M.; Dobson, P. J.; Grant, P. S. The Role of Nanomaterials in Redox-Based Supercapacitors for Next Generation Energy Storage Devices. *Nanoscale* **2011**, *3*, 839–855.
12. Lai, X.; Halpert, J. E.; Wang, D. Recent Advances in Micro-/Nano-Structured Hollow Spheres for Energy Applications: From Simple to Complex Systems. *Energy Environ. Sci.* **2012**, *5*, 5604–5618.
13. Guan, C.; Xia, X.; Meng, N.; Zeng, Z.; Cao, X.; Soci, C.; Zhang, H.; Fan, H. J. Hollow Core-Shell Nanostructure Supercapacitor Electrodes: Gap Matters. *Energy Environ. Sci.* **2012**, *5*, 9085–9090.
14. Lu, Q.; Lattanzi, M. W.; Chen, Y.; Kou, X.; Li, W.; Fan, X.; Unruh, K. M.; Chen, J. G.; Xiao, J. Q. Supercapacitor Electrodes with High-Energy and Power Densities Prepared from Monolithic NiO/Ni Nanocomposites. *Angew. Chem., Int. Ed.* **2011**, *50*, 6847–6850.
15. Zhou, C.; Zhang, Y.; Li, Y.; Liu, J. Construction of High-Capacitance 3d CoO@Polypyrrole Nanowire Array Electrode for Aqueous Asymmetric Supercapacitor. *Nano Lett.* **2013**, *13*, 2078–2085.
16. Lu, Z.; Chang, Z.; Zhu, W.; Sun, X. Beta-Phased $Ni(OH)_2$ Nanowall Film with Reversible Capacitance Higher Than Theoretical Faradic Capacitance. *Chem. Commun.* **2011**, *47*, 9651–9653.
17. Zhang, S.; Zeng, H. C. Self-Assembled Hollow Spheres of β-$Ni(OH)_2$ and Their Derived Nanomaterials. *Chem. Mater.* **2009**, *21*, 871–883.
18. Zhi, M.; Xiang, C.; Li, J.; Li, M.; Wu, N. Nanostructured Carbon-Metal Oxide Composite Electrodes for Supercapacitors: A Review. *Nanoscale* **2013**, *5*, 72–88.
19. Yuan, L. Y.; Yao, B.; Hu, B.; Huo, K. F.; Chen, W.; Zhou, J. Polypyrrole-Coated Paper for Flexible Solid-State Energy Storage. *Energy Environ. Sci.* **2013**, *6*, 470–476.
20. Xu, C.; Xu, B.; Gu, Y.; Xiong, Z.; Sun, J.; Zhao, G. Graphene-Based Electrodes for Electrochemical Energy Storage. *Energy Environ. Sci.* **2013**, *6*, 1388–1414.
21. Jiang, J.; Li, Y.; Liu, J.; Huang, X.; Yuan, C.; Lou, X. W. Recent Advances in Metal Oxide-Based Electrode Architecture Design for Electrochemical Energy Storage. *Adv. Mater.* **2012**, *24*, 5166–5180.
22. Reddy, A. L. M.; Gowda, S. R.; Shaijumon, M. M.; Ajayan, P. M. Hybrid Nanostructures for Energy Storage Applications. *Adv. Mater.* **2012**, *24*, 5045–064.
23. Cheng, C.; Fan, H. J. Branched Nanowires: Synthesis and Energy Applications. *Nano Today* **2012**, *7*, 327–343.
24. Mai, L.-Q.; Yang, F.; Zhao, Y.-L.; Xu, X.; Xu, L.; Luo, Y.-Z. Hierarchical $MnMoO_4/CoMoO_4$ Heterostructured Nanowires with Enhanced Supercapacitor Performance. *Nat. Commun.* **2011**, *2*, 381.
25. Xiao, X.; Li, T.; Peng, Z.; Jin, H.; Zhong, Q.; Hu, Q.; Yao, B.; Luo, Q.; Zhang, C.; Gong, L.; et al. Freestanding Functionalized Carbon Nanotube-Based Electrode for Solid-State Asymmetric Supercapacitors. *Nano Energy* **2014**, *6*, 1–9.
26. Xiao, X.; Peng, Z.; Chen, C.; Zhang, C.; Beidaghi, M.; Yang, Z.; Wu, N.; Huang, Y.; Miao, L.; Gogotsi, Y.; et al. Freestanding MoO_{3-X} Nanobelt/Carbon Nanotube Films for Li-Ion Intercalation Pseudocapacitors. *Nano Energy* **2014**, *9*, 355–363.
27. Xiao, X.; Ding, T.; Yuan, L.; Shen, Y.; Zhong, Q.; Zhang, X.; Cao, Y.; Hu, B.; Zhai, T.; Gong, L.; et al. WO_{3-X}/MoO_{3-X}core/Shell Nanowires on Carbon Fabric as an Anode for All-Solid-State Asymmetric Supercapacitors. *Adv. Energy Mater.* **2012**, *2*, 1328–1332.
28. He, Y.; Chen, W.; Li, X.; Zhang, Z.; Fu, J.; Zhao, C.; Xie, E. Freestanding Three-Dimensional Graphene/MnO_2 Composite Networks as Ultralight and Flexible Supercapacitor Electrodes. *ACS Nano* **2012**, *7*, 174–182.
29. Li, H. B.; Yu, M. H.; Wang, F. X.; Liu, P.; Liang, Y.; Xiao, J.; Wang, C. X.; Tong, Y. X.; Yang, G. W. Amorphous Nickel Hydroxide Nanospheres with Ultrahigh Capacitance and Energy Density as Electrochemical Pseudocapacitor Materials. *Nat. Commun.* **2013**, *4*, 1894.
30. Han, J.; Dou, Y.; Zhao, J.; Wei, M.; Evans, D. G.; Duan, X. Flexible Coal LDH@PEDOT Core/Shell Nanoplatelet Array for High-Performance Energy Storage. *Small* **2012**, *9*, 98–106.
31. Guan, C.; Zeng, Z.; Li, X.; Cao, X.; Fan, Y.; Xia, X.; Pan, G.; Zhang, H.; Fan, H. J. Atomic-Layer-Deposition-Assisted Formation of Carbon Nanoflakes on Metal Oxides and Energy Storage Application. *Small* **2014**, *10*, 300–307.
32. Yu, G.; Hu, L.; Liu, N.; Wang, H.; Vosgueritchian, M.; Yang, Y.; Cui, Y.; Bao, Z. Enhancing the Supercapacitor Performance of Graphene/MnO_2 Nanostructured Electrodes by Conductive Wrapping. *Nano Lett.* **2011**, *11*, 4438–4442.
33. Zhu, J.; Huang, L.; Xiao, Y.; Shen, L.; Chen, Q.; Shi, W. Hydrogenated CoO_x Nanowire @ $Ni(OH)_2$ Nanosheet Core-Shell Nanostructures for High-Performance Asymmetric Supercapacitors. *Nanoscale* **2014**, *6*, 6772–6781.
34. Stoller, M. D.; Ruoff, R. S. Best Practice Methods for Determining an Electrode Material's Performance for Ultracapacitors. *Energy Environ. Sci.* **2010**, *3*, 1294–1301.
35. Lu, X.; Yu, M.; Wang, G.; Tong, Y.; Li, Y. Flexible Solid-State Supercapacitors: Design, Fabrication and Applications. *Energy Environ. Sci.* **2014**, *7*, 2160–2181.
36. Yu, X.; Lu, B.; Xu, Z. Super Long-Life Supercapacitors Based on the Construction of Nanohoneycomb-Like Strongly Coupled $CoMoO_4$−3d Graphene Hybrid Electrodes. *Adv. Mater.* **2013**, *26*, 1044–1051.
37. Gogotsi, Y.; Simon, P. True Performance Metrics in Electrochemical Energy Storage. *Science* **2011**, *334*, 917–918.
38. liu, j.; Zhang, L. L.; Wu, H.; Lin, J.; Shen, Z.; Lou, D. X.-W. High-Performance Flexible Asymmetric Supercapacitors Based on a New Graphene Foam/Carbon Nanotubes Hybrid Film. *Energy Environ. Sci.* **2014**, *7*, 3709–3719.
39. Liu, J.; Chen, M.; Zhang, L.; Jiang, J.; Yan, J.; Huang, Y.; Lin, J.; Fan, H. J.; Shen, Z. X. A Flexible Alkaline Rechargeable Ni/Fe Battery Based on Graphene Foam/Carbon Nanotubes Hybrid Film. *Nano Lett.* **2014**, *14*, 7180–7187.
40. Wu, C.; Yin, P.; Zhu, X.; OuYang, C.; Xie, Y. Synthesis of Hematite (a-Fe_2O_3) Nanorods: Diameter-Size and Shape Effects on Their Applications in Magnetism, Lithium Ion Battery, and Gas Sensors. *J. Phys. Chem. B* **2006**, *110*, 17806–17812.
41. Yang, P.; Ding, Y.; Lin, Z.; Chen, Z.; Li, Y.; Qiang, P.; Ebrahimi, M.; Mai, W.; Wong, C. P.; Wang, Z. L. Low-Cost High-Performance Solid-State Asymmetric Supercapacitors Based on MnO_2 Nanowires and Fe_2O_3 Nanotubes. *Nano Lett.* **2014**, *14*, 731–736.
42. Long, C.; Wei, T.; Yan, J.; Jiang, L.; Fan, Z. Supercapacitors Based on Graphene-Supported Iron Nanosheets as Negative Electrode Materials. *ACS Nano* **2013**, *7*, 11325–11332.
43. Sassin, M. B.; Mansour, A. N.; Pettigrew, K. A.; Rolison, D. R.; Long, J. W. Electroless Deposition of Conformal Nanoscale Iron Oxide on Carbon Nanoarchitectures for Electrochemical Charge Storage. *ACS Nano* **2010**, *4*, 4505–4514.
44. Li, X.; Fan, N. C.; Fan, H. J. A Micro-Pulse Process of Atomic Layer Deposition of Iron Oxide Using Ferrocene and Ozone Precursors and Ti-Doping. *Chem. Vapor Depos.* **2013**, *19*, 104–110.
45. Ramachandran, R. K.; Dendooven, J.; Detavernier, C. Plasma Enhanced Atomic Layer Deposition of Fe_2O_3 Thin Films. *J. Mater. Chem. A* **2014**, *2*, 10662–10667.
46. Elam, J. W.; Dasgupta, N. P.; Prinz, F. B. Ald for Clean Energy Conversion, Utilization, and Storage. *MRS Bull.* **2011**, *36*, 899–906.
47. Marichy, C.; Bechelany, M.; Pinna, N. Atomic Layer Deposition of Nanostructured Materials for Energy and Environmental Applications. *Adv. Mater.* **2012**, *24*, 1017–1032.

48. Meng, X.; Yang, X.-Q.; Sun, X. Emerging Applications of Atomic Layer Deposition for Lithium-Ion Battery Studies. *Adv. Mater.* **2012**, *24*, 3589–3615.
49. Knez, M.; Nielsch, K.; Niinistö, L. Synthesis and Surface Engineering of Complex Nanostructures by Atomic Layer Deposition. *Adv. Mater.* **2007**, *19*, 3425–3438.
50. Wang, D.; Li, Y.; Wang, Q.; Wang, T. Nanostructured Fe_2O_3–Graphene Composite as a Novel Electrode Material for Supercapacitors. *J. Solid State Electrochem.* **2012**, *16*, 2095–2102.
51. Qu, Q.; Yang, S.; Feng, X. 2d Sandwich-Like Sheets of Iron Oxide Grown on Graphene as High Energy Anode Material for Supercapacitors. *Adv. Mater.* **2011**, *23*, 5574–5580.
52. Martinson, A. B. F.; DeVries, M. J.; Libera, J. A.; Christensen, S. T.; Hupp, J. T.; Pellin, M. J.; Elam, J. W. Atomic Layer Deposition of Fe_2O_3 Using Ferrocene and Ozone. *J. Phys. Chem. C* **2011**, *115*, 4333–4339.
53. Klahr, B. M.; Martinson, A. B. F.; Hamann, T. W. Photoelectrochemical Investigation of Ultrathin Film Iron Oxide Solar Cells Prepared by Atomic Layer Deposition. *Langmuir* **2010**, *27*, 461–468.
54. Boukhalfa, S.; Evanoff, K.; Yushin, G. Atomic Layer Deposition of Vanadium Oxide on Carbon Nanotubes for High-Power Supercapacitor Electrodes. *Energy Environ. Sci.* **2012**, *5*, 6872–6879.
55. Marichy, C.; Tessonnier, J.-P.; Ferro, M. C.; Lee, K.-H.; Schlogl, R.; Pinna, N.; Willinger, M.-G. Labeling and Monitoring the Distribution of Anchoring Sites on Functionalized CNTs by Atomic Layer Deposition. *J. Mater. Chem.* **2012**, *22*, 7323–7330.
56. Marichy, C.; Russo, P. A.; Latino, M.; Tessonnier, J.-P.; Willinger, M.-G.; Donato, N.; Neri, G.; Pinna, N. Tin Dioxide–Carbon Heterostructures Applied to Gas Sensing: Structure-Dependent Properties and General Sensing Mechanism. *J. Phys. Chem. C* **2013**, *117*, 19729–19739.
57. Meng, X.; Ionescu, M.; Banis, M.; Zhong, Y.; Liu, H.; Zhang, Y.; Sun, S.; Li, R.; Sun, X. Heterostructural Coaxial Nanotubes of CNT@Fe_2O_3 *Via* Atomic Layer Deposition: Effects of Surface Functionalization and Nitrogen-Doping. *J. Nanopart. Res.* **2011**, *13*, 1207–1218.
58. Chen, X.; Zhu, H.; Chen, Y.-C.; Shang, Y.; Cao, A.; Hu, L.; Rubloff, G. W. MWCNT/V_2O_5 Core/Shell Sponge for High Areal Capacity and Power Density Li-Ion Cathodes. *ACS Nano* **2012**, *6*, 7948–7955.
59. George, S. M. Atomic Layer Deposition: An Overview. *Chem. Rev.* **2009**, *110*, 111–131.
60. Wang, H.; Xu, Z.; Yi, H.; Wei, H.; Guo, Z.; Wang, X. One-Step Preparation of Single-Crystalline Fe_2O_3 Particles/Graphene Composite Hydrogels as High Performance Anode Materials for Supercapacitors. *Nano Energy* **2014**, *7*, 86–96.
61. Jiang, C.; Hosono, E.; Zhou, H. Nanomaterials for Lithium Ion Batteries. *Nano Today* **2006**, *1*, 28–33.
62. Wang, H.; Liang, Y.; Gong, M.; Li, Y.; Chang, W.; Mefford, T.; Zhou, J.; Wang, J.; Regier, T.; Wei, F.; et al. An Ultrafast Nickel–Iron Battery from Strongly Coupled Inorganic Nanoparticle/Nanocarbon Hybrid Materials. *Nat. Commun.* **2012**, *3*, 917.
63. Jiang, W.; Liang, F.; Wang, J.; Su, L.; Wu, Y.; Wang, L. Enhanced Electrochemical Performances of FeO_x-Graphene Nanocomposites as Anode Materials for Alkaline Nickel-Iron Batteries. *RSC Adv.* **2014**, *4*, 15394–15399.
64. Liu, Z.; Tay, S. W.; Li, X. Rechargeable Battery Using a Novel Iron Oxide Nanorods Anode and a Nickel Hydroxide Cathode in an Aqueous Electrolyte. *Chem. Commun.* **2011**, *47*, 12473–12475.
65. Xu, H.; Hu, X.; Yang, H.; Sun, Y.; Hu, C.; Huang, Y. Flexible Asymmetric Micro-Supercapacitors Based on Bi_2O_3 and MnO_2 Nanoflowers: Larger Areal Mass Promises Higher Energy Density. *Adv. Energy Mater.* **2014**, 10.1002/aenm.201401882.